MIT Libraries | DSpace@MIT

MIT Open Access Articles

Unifying first-principles theoretical predictions and experimental measurements of size effects in thermal transport in SiGe alloys

Massachusetts Institute of Technology

Unifying first principle theoretical predictions and experimental measurements of size effects in thermal transport in SiGe alloys

Samuel Huberman,[1] Vazrik Chiloyan,[1] Ryan A. Duncan,[2] Lingping Zeng,[1] Roger Jia,[3]

Alexei A. Maznev,[2] Eugene A. Fitzgerald,[3] Keith A. Nelson,[2] and Gang Chen[1, *]

[1]*Department of Mechanical Engineering,*

Massachusetts Institute of Technology,

Cambridge, Massachusetts 02139, USA

[2]*Department of Chemistry, Massachusetts Institute of Technology,*

Cambridge, Massachusetts 02139, USA

[3]*Department of Materials Science and Engineering,*

Massachusetts Institute of Technology,

Cambridge, Massachusetts 02139, USA

(Dated: September 8, 2017)

Abstract

We demonstrate the agreement between first principle calculations and experimental measurements of size effects in thermal transport in SiGe alloys without fitting parameters. Transient thermal grating (TTG) is used to measure the effect of grating period on the temperature decay. The virtual crystal approximation under the density functional theory framework combined with impurity scattering is used to determine the phonon properties for the exact alloy composition of the measured samples. With these properties, classical size effects are calculated for the experimental geometry of reflection mode TTG using the recently-developed variational solution to the phonon Boltzmann transport equation, which is verified against established Monte Carlo simulations. We find agreement between theoretical predictions and experimental measurements in the reduction of thermal conductivity (as much as 4-fold of the bulk value) across grating periods spanning one order of magnitude. This paper provides a framework for the study of size effects in thermal transport in opaque materials.

* gchen2@mit.edu

I. INTRODUCTION

Deviations from the Fourier regime of thermal transport occur when length scales become on the order of the mean free paths of thermal energy carriers. Geometries where the dimensions of heating or sample size can be shrunk to such a scale have provided experimentalists with a tool for probing size effects in thermal transport. For instance, Hu et al. used nanoscale metal heaters exposed to optical heating in the time domain thermoreflectance (TDTR) configuration to measure size effects in bulk substrates [1] and Cuffe et al. used the transmission mode transient thermal grating (TTG) geometry to study the effect of film thickness in silicon membranes [2].

The nano-heater technique requires careful fabrication and microscopic knowledge of the thermal interface between the heaters and substrate for an accurate description of the transport. The transmission TTG requires optically thin and mechanically free membranes, limiting the range of materials that can be studied. Thus, a technique which overcomes these disadvantages is desirable. First used by Johnson et al. to observe non-diffusive transport in GaAs [3], the reflection mode TTG technique is a simple geometry that is not obfuscated by an interface or limited to thin membranes. The objective of this work is to use a bottom up theoretical approach and apply the framework to the reflection mode TTG. In doing so, we are able to unify the pictures obtained from the macroscopic observables of experiment to the microscopic properties from theory.

Our candidate material is a silicon-germanium (SiGe) alloy, as this system has proven to be a canonical case for the study of thermal transport in a mass-disordered, yet crystalline system, evidenced by the plethora of work, dating back to the original work by Stohr [4], Toxen [5] and Abeles [6, 7], where it was noted that the mass-disorder scatters short-wavelength phonons consequently shifting the dominant contribution to thermal conductivity to long wavelength phonons.

The concept of large contribution to thermal conductivity from long wavelength phonons with large mean free paths (MFP) was used to explain the observation from Koh et al., who reported a modulation frequency dependent estimate of thermal conductivity under the Fourier model of the experimental geometry of TDTR [8]. The authors suggested that the frequency dependence corresponds to a reduction in the contribution to thermal conductivity of the large MFP phonons. This result led to a series of theoretical explanations [9–13].

However, each of these explanations invoked a set of fitting parameters to accurately capture the experimental observable.

Inspired by the multiple theoretical attempts to explain the experimental observations, we present theoretical predictions that accurately capture our experimental observables without relying upon fitting parameters or unnecessary approximations. The structure of the paper is as follows. In Section II we present the phonon properties obtained using density functional theory. In Section II B, the variational solution to the phonon BTE for the TTG experimental geometry is developed. In Section III, results obtained from TTG are presented and compared with our BTE-based predictions. Finally, we close with a discussion and outlook in Section IV.

II. THEORY

A. First Principle Calculations

We follow the general procedure established by Broido [14, 15] and Esfarjani [16], to obtain the phonon properties for SiGe. While the details can be found in these works, an outline of the procedure is included for the sake of completeness.

For a non-alloy system, the harmonic phonon properties are obtained using density-functional perturbation theory (DFPT). The underlying premise is to treat the mechanical displacement corresponding the wavevector of a phonon as a linear perturbation to the electronic Hamiltonian, from which atomic forces can be calculated under the self-consistent criteria of DFT. These forces are then converted into harmonic force constants and used to construct the dynamical matrix for the perturbing wavevector, which can then be diagonalized to obtain the corresponding frequencies. The anharmonic properties can be obtained by extending the perturbation to higher orders [17]. The approach we follow begins with constructing a symmetry-reduced set of atomic displacements in a supercell, where each member of the set undergoes a standard DFT self-consistent calculation, each yielding the force field for the configuration. With this set of force fields, the third order force constants are extracted. Phonon lifetimes are related to the third order force constants through the application of Fermi's golden rule. Integrating the modal thermal conductivity over the Brillouin zone, under the relaxation time approximation to the phonon BTE, yields the lattice

thermal conductivity. This full procedure is implemented in the ShengBTE package [18].

To extend the above procedure to a crystalline alloy, approximations are necessary. As discussed by Toxen [5] and Abeles [6], the SiGe alloys are ideal candidates for studying the validity of the VCA. Following Garg et al. [19], we use the VCA to modify the DFT calculations. Within this approximation, two paths can be taken. One can compositionally average the pseudopotentials for the constituent atoms, and then proceed with the usual procedure. Alternatively, one can calculate the harmonic and third order force constants for the unalloyed crystalline versions of the constituent atoms, take the mass normalized compositional average and then proceed to calculate the phonon properties:

$$A_{VCA} = xA^{Si} + (1-x)A^{Ge} \tag{1}$$

where x is the percent composition of silicon and A^i is a placeholder for the harmonic force constants, the third order force constants, the atomic masses and the lattice constants [20] of the constituent atoms. We have followed both VCA procedures, and find negligible difference in the phonon properties (see supplementary material).

The penultimate step in the alloy calculation is to include the effect of mass disorder. Again, following Garg's work, the phonon lifetimes are modified under Matthiessen's rule using the theory established by Tamura [21] to treat isotope scattering as an elastic perturbation. Garg et al. went a step further to estimate the anharmonic shifts do due disorder through supercell calculations. Feng et al. used molecular dynamics to show that the application of Matthiessen's rule leads to an overestimation of thermal conductivity by more than $\sim 20\%$ in SiGe due to neglecting four and five-phonon processes [22]. Our experimental results will show that the harmonic mass disorder approximation under Matthiessen's rule produces reasonable theoretical predictions. We note that the procedure followed in this work will not capture the frequency shifts that can be observed in the SiGe Raman spectra [23, 24] (see supplementary material). It is expected that these Raman active modes do not significantly contribute to thermal conductivity, as their group velocities are small and their lifetimes have been reduced by mass disorder scattering. The phonon properties are reported in Figure 1 and details of the DFT calculations are available in the supplementary material.
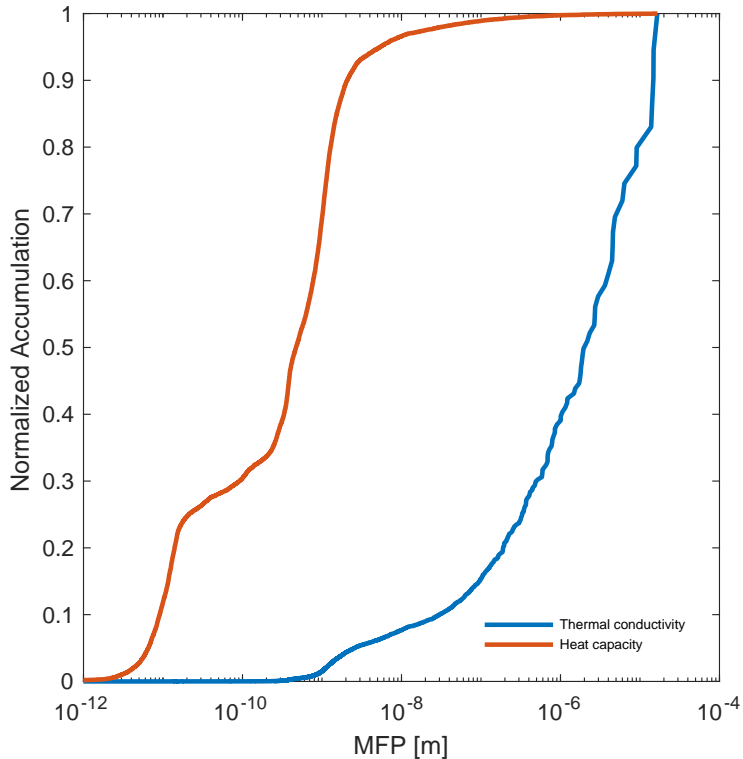
FIG. 1: $Si_{93.4}Ge_{6.6}$ MFP accumulation of thermal conductivity and heat capacity at 300 K.

B.   Solving the Boltzmann Transport Equation

Given the bulk phonon properties of $Si_{93.4}Ge_{6.6}$, we now turn to the study of the effect of grating period length on thermal transport in the reflection mode TTG geometry. The diffusive temperature profile has previously been obtrained in order to analyze the temperature signal using TTG for opaque materials [25]. For the experimental conditions of a spatially periodic heat source defined by wavevector $q = \frac{2\pi}{\lambda}$, the temperature is given by $T(x, z, t) = T_0 + T_0 e^{iqx} h(z, t)$ in complex form, and this serves as a definition of the non-dimensional temperature h. The temperature T_0 is the background equilibrium temperature of the system, for example the room temperature. The heating by the laser is incorporated with a volumetric heat generation term, given by the functional form:

$$Q = \delta(t)\mathrm{e}^{iqx}U_0\beta\mathrm{e}^{-\beta z} \tag{2}$$

where U_0 represents the energy per unit area deposited into the substrate by the pulse, and β is the inverse penetration depth of the heating profile. The derivation found in [25] takes

5

into consideration different in-plane and cross-plane thermal conductivities, however the experimental signal is mostly sensitive to the in-plane thermal conductivity. For simplicity, we show the derivation for an isotropic system, where the Fourier heat conduction equation simplifies to:

$$\frac{\partial h}{\partial t} = -\alpha q^2 h + \alpha \frac{\partial^2 h}{\partial z^2} + \frac{\beta U_0}{CT_0} e^{-\beta z} \delta(t) \tag{3}$$

with the initial and boundary conditions given by:

$$h(z, t = 0^-) = 0$$
$$\frac{\partial h}{\partial z}\Big|_{z=0} = 0 \tag{4}$$
$$h(z \to \infty, t) = 0$$

which assumes an adiabatic surface at $z = 0$, and that the system starts at equilibrium prior to the energy deposited by the laser. We present the solution in the Laplace transformed domain for convenience:

$$\hat{h}(z, s) = \frac{\frac{\beta U_0}{CT_0}}{s + \alpha(q^2 - \beta^2)} \left(e^{-\beta z} - \frac{\beta}{\sqrt{q^2 + \frac{s}{a}}} e^{-z\sqrt{q^2 + \frac{s}{a}}} \right) \tag{5}$$

We intend to utilize this Fourier heat conduction temperature profile in our variational solution of the BTE. Taking the inverse Laplace transform of this yields the temperature as a function of the depth into the substrate and time:

$$h(z, t) = \frac{\beta U_0}{2CT_0} e^{-\alpha t(q^2 - \beta^2)} \left(e^{\beta z} \mathrm{erfc}(\beta\sqrt{\alpha t} + \frac{z}{2\sqrt{\alpha t}}) + e^{-\beta z} \mathrm{erfc}(\beta\sqrt{\alpha t} - \frac{z}{2\sqrt{\alpha t}}) \right) \tag{6}$$

where the surface temperature is:

$$h(z = 0, t) = \frac{\beta U_0}{CT_0} e^{-\alpha t(q^2 - \beta^2)} \mathrm{erfc}(\beta\sqrt{\alpha t}) \tag{7}$$

1. Temperature integral equation

We begin with the spectral Boltzmann transport equation under the relaxation time approximation (RTA):

$$\frac{\partial g_\omega}{\partial t} + \mathbf{v}_\omega \cdot \nabla g_\omega = \frac{g_0 - g_\omega}{\tau_\omega} + \frac{Q_\omega}{4\pi} \tag{8}$$

where g_ω is the phonon energy density per unit frequency interval per unit solid angle above the reference background energy, related to the distribution function as $g_\omega = \frac{\hbar\omega D(\omega)}{4\pi}(f_\omega - f_0(T_0))$. $\mathbf{v}_\omega$ is the group velocity, τ_ω is the relaxation time, and g_0 is the equilibrium energy density, given by $g_0 \approx \frac{1}{4\pi}C_\omega(T - T_0)$ in the linear response regime. The sinusoidal heating profile in the x-direction (in-plane), given by the pulse form $Q_\omega(x, z, t) = \delta(t)e^{iqx}\tilde{Q}_\omega(z)$, means we can expect that the spectral and equilibrium energy densities to also obey a sinusoidal profile $g_\omega = e^{iqx}\tilde{g}_\omega$ and the equilibrium distribution will simplify accordingly to $\tilde{g}_0 = \frac{C_\omega T_0}{4\pi}h(z, t)$. By inputting this in-plane sinusoidal profile and utilizing the Laplace transform (denoted by the ^ symbol) in the time domain, the BTE simplifies to:

$$\frac{\partial \hat{\tilde{g}}_\omega}{\partial z} + \hat{\tilde{g}}_\omega \frac{1 + s\tau_\omega + i\eta_\omega\mu_x}{\Lambda_\omega\mu_z} = \frac{\hat{\tilde{g}}_0 + \tau_\omega\frac{\tilde{Q}_\omega}{4\pi}}{\Lambda_\omega\mu_z} \tag{9}$$

where we have defined $\eta_\omega = q\Lambda_\omega$. For convenience, we define the parameter $V = \frac{1 + s\tau_\omega + i\eta_\omega\mu_x}{\Lambda_\omega\mu_z}$ to group the variables in a compact form for the following solution of the BTE:

$$\hat{\tilde{g}}_\omega(z, s, \mu_x, \mu_z) = e^{-Vz}\hat{\tilde{g}}_\omega(z = 0, s, \mu_x, \mu_z) + \int_0^z dz' e^{-V(z-z')} \frac{\hat{\tilde{g}}_0(z', s) + \tau_\omega\frac{\tilde{Q}_\omega}{4\pi}}{\Lambda_\omega\mu_z} \tag{10}$$

The boundary conditions are taken to be:

$$\hat{\tilde{g}}_\omega(z = L, s, \mu_x, \mu_z < 0) = 0$$
$$\hat{\tilde{g}}_\omega(z = 0, s, \mu_x, \mu_z > 0) = \sigma \tag{11}$$

The first boundary condition takes an imaginary blackbody wall at length L into the substrate at the background temperature to account for the semi-infinite substrate, where this length approaches infinity. The second boundary condition provides the adiabatic boundary condition with diffuse scattering, where $\sigma = \frac{1}{\pi}\int d\Omega\Theta(\mu_z)\mu_z\hat{\tilde{g}}_\omega(z = 0, s, \mu_x, -\mu_z)$, which is proportional to the specular heat flux approaching the surface. We have utilized the Heaviside step function to reduce the integration over the solid angle only to consider phonons approaching the surface. Applying the boundary conditions, and taking the artificial length L to infinity yields the formal solution to the BTE for the spectral energy density in terms of the equilibrium energy density:

$$\hat{\tilde{g}}_\omega(z,s,\mu_x,\mu_z) = -\Theta(-\mu_z)\int_z^\infty e^{-V(z-z')}\frac{\hat{\tilde{g}}_0(z',s)+\tau_\omega\frac{\tilde{Q}_\omega}{4\pi}}{\Lambda_\omega\mu_z}$$
$$+\Theta(\mu_z)\left(\int_0^z e^{-V(z-z')}\frac{\hat{\tilde{g}}_0(z',s)+\tau_\omega\frac{\tilde{Q}_\omega}{4\pi}}{\Lambda_\omega\mu_z}+\int_0^\infty 2e^{-V(z)}F_2(z')\frac{\hat{\tilde{g}}_0(z',s)+\tau_\omega\frac{\tilde{Q}_\omega}{4\pi}}{\Lambda_\omega}\right)$$

$$(12)$$

where we have defined the following solid angle integral function:

$$F_n(z) = \frac{1}{2\pi}\int d\Omega\,\Theta(\mu_z)\mu_z^{n-2}(e)^{-Vz} \tag{13}$$

The first term represents phonons moving towards the surface of heating at $z = 0$, whereas the second term represents phonons moving away from the surface.

The temperature can be derived by utilizing the equilibrium condition obtained by integrating Eq. 12 with respect to frequency and the solid angle [26]. The equilibrium condition in this case can be expressed as:

$$4\pi\int d\omega\frac{1}{\tau_\omega}\hat{\tilde{g}}_0(z,s) = \int d\omega\frac{1}{\tau_\omega}\int d\Omega\,\hat{\tilde{g}}_\omega(z,s,\mu_x,\mu_z) \tag{14}$$

Performing the solid angle integral, and inputting the expression for the non-dimensional temperature expression $\hat{\tilde{g}}_0 = \frac{C_\omega T_0}{4\pi}\hat{h}(z,s)$, we obtain the integral equation for the temperature distribution:

$$\hat{h}(z,s)\int d\omega\frac{C_\omega}{\tau_\omega} = \int d\omega\frac{C_\omega}{2\Lambda_\omega\tau_\omega}\int_0^\infty dz'\left(\hat{h}(z',s)+\frac{\tau_\omega\tilde{Q}_\omega(z')}{C_\omega T_0}\right)(F_1(|z-z'|)+2F_2(z)F_2(z')) \tag{15}$$

This is an integral equation in the spatial variable z for the non-dimensional temperature in the Laplace domain, which after solving, requires an inverse Laplace transform in order to obtain the full temperature solution in the time domain. For the thermal distribution, the spectral heat generation takes the form:

$$\tilde{Q}_\omega(z) = \frac{C_\omega}{C}U_0\beta e^{-\beta z} \tag{16}$$

Note that $\frac{C_\omega}{C}$ is a weighting of the contribution of a given mode to heat generation under the assumption of thermalized distribution [27]. While other distributions can be taken, we utilize this form in order to compare to the Fourier heat conduction solution.

8

2. *Variational solution*

Eq. 15 can be numerically solved using finite difference methods [28] or Monte Carlo methods [29, 30]. In this work, we extend a variational approach previously presented for the 1D TTG [31] and thin film TTG geometries [32] to the reflection mode TTG geometry. The starting point of this approach is to select a trial function. The simplest trial function is to take the diffusive temperature profile and allow just the thermal diffusivity to be a variational parameter. In general, the size effects exhibited by the BTE will affect both the temporal as well as the spatial distributions of the temperature. However, the simple variational solution that varies only one parameter, the thermal diffusivity, performs well by approximately solving for the thermal decay from the BTE over a broad range of grating period length scales. We proceed by taking the Fourier heat conduction solution of Eq. 5 as a trial function and use the thermal diffusivity as the variational parameter.

To solve for the variational parameter, we can utilize mathematical optimization methods such as least squares on the error residual of the temperature equation [31], or impose a physical condition that we wish the trial function to satisfy. Here, we impose that the trial function must satisfy energy conservation taken over the control volume of the semi-infinite substrate over all time, analogous to the condition utilized for the thin film TTG geometry [32]. This mathematical condition can be obtained by integrating the BTE of Eq. 14 over the solid angle and frequency, and then also over the depth variable z as well as over all time to yield:

$$U_0 \frac{\lambda}{\pi} = 2i \int_0^\infty dz \int_0^\infty dt \tilde{q}_x(z,t) \tag{17}$$

This statement says that the total energy per unit area perpendicular to the z-axis deposited in the semi-infinite substrate initially (left hand side of Eq. 16) must be equal to the total energy that moves away in the in-plane direction. The in-plane heat flux is obtained by utilizing the spectral energy density of Eq. 12, and integrating over the frequency and solid angle $\hat{\tilde{q}}_x(z,s) = \int d\omega \int d\Omega \Theta v_\omega \mu_x \hat{\tilde{g}}_\omega(z,s,\mu_x,\mu_z)$ to obtain the in-plane heat flux:

$$\hat{\tilde{q}}_x(z,s) = \frac{T_0}{2} \int d\omega \frac{C_\omega v_\omega}{\Lambda_\omega} \int_0^\infty dz' \left(\hat{h}(z',s) + \frac{\tau_\omega \tilde{Q}_\omega(z')}{C_\omega T_0} \right) (G_1(|z-z'|) + 2G_2(z)F_2(z')) \tag{18}$$

where we have defined the solid angle integral function:

9

$$G_n(z) = \frac{1}{2\pi} \int d\Omega \Theta(\mu_z) \mu_z^{n-2} \mu_x(e)^{-Vz} \tag{19}$$

Inserting the heat flux expression of Eq. 18 into the energy conservation statement of Eq. 17, and inputting the variational trial function of the Fourier heat conduction solution of Eq. 5 as well as the thermal distribution for the heat generation rate, we can solve for the effective thermal conductivity after cleaning up some of the solid angle integrals. We obtain a form similar in structure to the results from the thin film TTG [32] and the one-dimensional limit of the TTG [31]:

$$k = \frac{\frac{1}{3} \int d\omega C_\omega v_\omega \Lambda_\omega f(\eta_\omega, \mathrm{Kn}_\omega)}{\frac{1}{C} \int d\omega C_\omega g(\eta_\omega, \mathrm{Kn}_\omega)} \tag{20}$$

where $\mathrm{Kn}_\omega = \Lambda_\omega \beta$. Note that information concerning the spectral contribution to heat capacity is needed in the equation for effective thermal conductivity [33]. f and g are the kernels that weigh a given mode's contribution to effective thermal conductivity under the imposed size effects, explicitly given as

$$f(\eta_\omega, \mathrm{Kn}_\omega) = \frac{3}{\eta_\omega^2} \left(1 - \frac{1}{\eta_\omega} \arctan(\eta_\omega) + \frac{\eta_\omega^2 \Psi(\eta_\omega, \mathrm{Kn}_\omega) - \mathrm{Kn}_\omega^2 \Psi(\eta_\omega, \mathrm{Kn}_\omega)}{\eta_\omega^2 - \mathrm{Kn}_\omega^2} \right)$$
$$g(\eta_\omega, \mathrm{Kn}_\omega) = \frac{1}{\eta_\omega} \arctan(\eta_\omega) + \Psi(\eta_\omega, \mathrm{Kn}_\omega) \tag{21}$$

We have defined the following solid angle integral functions:

$$\Psi(x, z) = \frac{1}{2} \psi_1(x, z) - \frac{1}{1 + \sqrt{1 + x^2}} \psi_0(x, z)$$
$$\psi_n(x, z) = \frac{1}{2\pi} \int d\Omega \Theta(\mu_z) \frac{z\mu_z}{(1 + ix\mu_x)^n (1 + z\mu_z + ix\mu_x)} \tag{22}$$

If we take the limit of $\mathrm{Kn}_\omega \to 0$, i.e. the case of very long penetration depth, the solid angle integrals vanish as $\psi_n(\eta_\omega, \mathrm{Kn}_\omega \to 0) \propto \mathrm{Kn}_\omega$, and we recover the one-dimensional TTG limit described by the previously derived effective thermal conductivity [31]. The more interesting case for this problem is the reduction to surface heating, i.e. $\mathrm{Kn}_\omega \to \infty$. In this case, the kernel functions simplify to:

$$f(\eta_\omega, \mathrm{Kn}_\omega \to \infty) = \frac{3}{2\eta_\omega^2}\left(1 - \frac{1}{\eta_\omega}\arctan(\eta_\omega)\right) - \frac{1}{\eta_\omega^3(1+\sqrt{1+\eta_\omega^2})}\left((1+\eta_\omega)^{\frac{3}{2}} - \frac{3}{2}\eta_\omega^2 - \eta_\omega^3 - 1\right)$$

$$g(\eta_\omega, \mathrm{Kn}_\omega \to \infty) = \frac{1}{2\eta_\omega}\arctan(\eta_\omega) + \frac{1}{1+\sqrt{1+\eta_\omega^2}}$$

$$(23)$$

For the general case of arbitrary penetration depth, the solid angle integral functions can be calculated analytically (available in the supplementary material), which allows for a fully analytical effective thermal conductivity for any penetration depth into the substrate.

3. Comparison between the Variational Solution and Monte Carlo Simulations

To study the effect of the optical penetration depth in the case of a diffuse surface boundary condition, we first plot the kernels f and g as a function of η for the extremal limits of Kn_ω. The one-dimensional limit of $\mathrm{Kn}_\omega \to 0$ and the surface heating limit of $\mathrm{Kn}_\omega \to \infty$ define the envelope of curves for which the kernels for arbitrary values of the penetration depth must lie between. As the Knudsen number increases, the size effect due to the optical penetration depth increases, which physically results in a decrease of the effective thermal conductivity. This occurs due to the decrease in the numerator kernel f, and the increase of the denominator kernel g. However, the variational solution produces a one-dimensional limit and the surface heating limit that are practically indistinguishable (Figure 2), suggesting that the effective thermal conductivity due to a diffuse boundary experiences weak effects from the optical penetration depth.

Utilizing the derived kernels to calculate the effective thermal conductivity for $\mathrm{Si}_{93.4}\mathrm{Ge}_{6.6}$, we show in Figure 3 the effective thermal conductivity in the various limits. Note that the effective thermal conductivity is quite similar in the one-dimensional limit and in the surface heating limit. As expected, when the thermal grating period is much smaller than the optical penetration depth, the effective thermal conductivity takes on values of the one-dimensional limit, as the transport is mostly in-plane. In the opposite case, when the grating period is much larger than the optical penetration depth, the effective thermal conductivity approaches the surface heating limit.

Figure 3 demonstrates that the variational technique predicts that transport has a weak dependence on the optical penetration depth, a consequence of the kernels' weak depen-
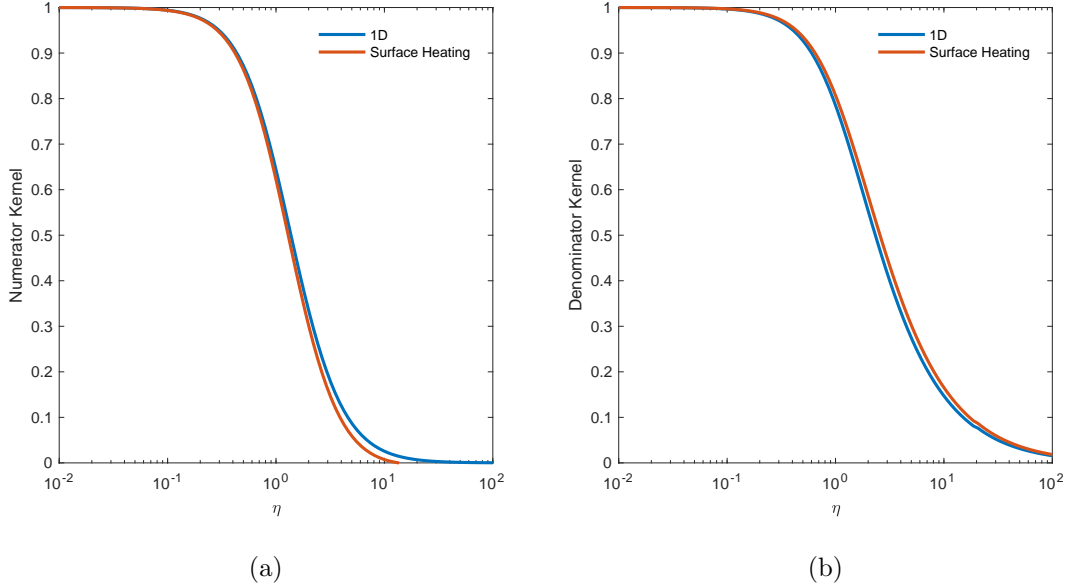
FIG. 2: Kernels of the effective conductivity in Eq. 20. (a) The numerator kernel f that shows the size effects and appears beside the differential conductivity and (b) the denominator kernel g that shows the size effects and appears beside the spectral heat capacity.

dence on optical penetration depth. In the limit of $q/\beta \gg 1$, the one dimensional TTG is recovered. In the limit of $q/\beta \ll 1$, the modified Fourier approach fails to capture the short time behavior. In this regime, the use of effective thermal conductivity (obtained either using the variational approach or otherwise) is insufficient to characterize thermal transport. An example of this failure is presented in the supplementary material. Even with such a limitation, our variational approach sufficiently characterizes the intermediate regime.

In the limit of $q/\beta \ll 1$, the variational method, using the Fourier temperature profile as input, reveals that the thermal conductivity that best recovers this behavior is the bulk value. This can be understood as a consequence of the constraint imposed by the equilibrium condition of Eq. 17, which dictates the behavior of the variational temperature profile in the large time limit where transport is diffusive. To ensure that this limitation is not present in the current experimental study, we compare against established Monte Carlo simulations of the RTA-BTE [29, 30].

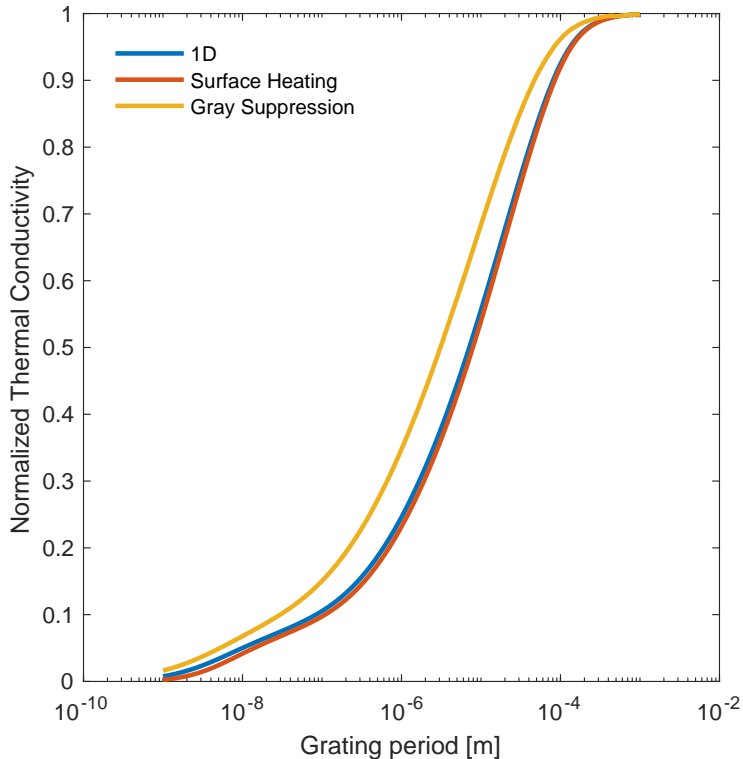As is seen in Figure 4, agreement at a grating period of 100 nm and an optical penetration

12

FIG. 3: Effective thermal conductivity for $Si_{93.4}Ge_{6.6}$ in the one-dimensional limit and the surface heating limit. The effective thermal conductivity using the gray suppression function for one-dimensional TTG (Eq. 24) is also shown [31].

depth of 10 nm and for a grating period of 10 μm and an optical penetration depth of 1 um is observed. As our experiments have penetration depths on the order of 1 μm for $Si_{93.4}Ge_{6.6}$ [34], and use grating periods of between 1 and 13.5 μm, we are not in the $q/\beta \ll 1$ regime and we can move forward with our variational solutions.

III. EXPERIMENT

A. Sample specifications

The SiGe sample was fabricated by metal-organic chemical vapor deposition (MOCVD). Briefly, SiH_4 and GeH_4 enter the reactor, which break up into Si, Ge, and H_2 from exposure to high temperatures (750-800C). The composition is controlled by tunning the flow rates of SiH_4 and GeH_4. A single crystal sample consisting of 93.4% Si, 6.6% Ge with a thickness
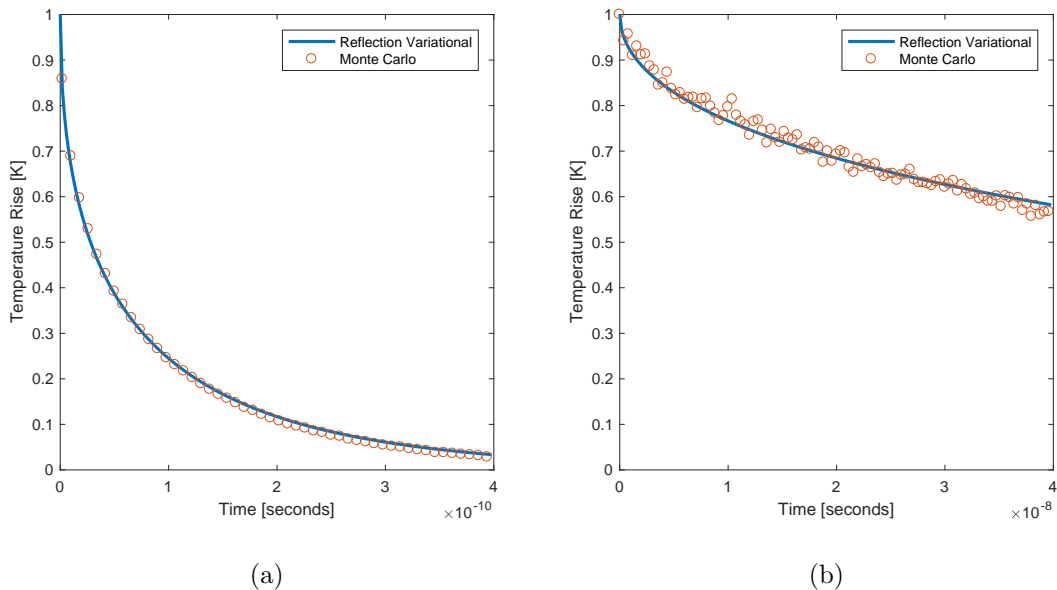
FIG. 4: Temperature profiles obtained from Monte Carlo simulations compared with the corresponding variational predictions for $Si_{93.4}Ge_{6.6}$ at 300 K with a (a) grating period of 100 nm and optical penetration depth of 10 nm and a (b) grating period of 10 μm and optical penetration depth of 1 μm. The Monte Carlo trace for case (b) contains noise because of the computational cost of simulating longer decays for a large number of effective particles. The Monte Carlo source code is included in the supplementary material.

of 6 um on a [1 0 0] oriented Si wafer with 6 degree off-cut towards the [1 1 1] plane was used for this work. Details of the sample fabrication and characterization can be found in previous work [35].

B. Transient Thermal Grating Measurements

Transient grating spectroscopy is a variant on four-wave-mixing spectroscopic techniques that can measure thermal transport dynamics over a well-defined in-plane length scale. In this technique, two pump laser pulses (515 nm, 60 ps FWHM) are crossed at the surface of the sample, where they interfere to yield a sinusoidal intensity pattern. Absorption by the sample creates a matching temperature profile, which evolves as a function of time through in-plane and cross-plane transport. The time dynamics of this "transient grating" are measured by the diffraction of a quasi-continuous probe beam (532 nm), and phase-specific information is

extracted through heterodyned detection of the TTG signal by superposition of the diffracted signal with a reference beam (local oscillator) derived from the probe beam source. The signal is detected using a fast photodiode (1 GHz bandwidth) and recorded on an oscilloscope (4GHz bandwidth). Specific details of the optical setup can be found elsewhere [25, 36, 37] and a depiction of the TTG setup is shown in Figure 5.
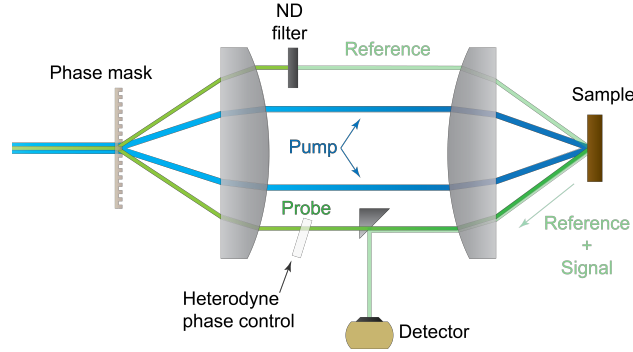

FIG. 5: A diagram of the reflection mode TTG geometry. The pump and probe beams are passed through the diffraction grating (referred to here as the phase mask), the which sets the period length of the heating profile. The ± 1 orders of the pump and probe are then imaged on the sample surface using the $4f$ lens system. An ND filter attenuates the reference beam of the probe, while an optic (the heterodyne phase control) is placed in the signal beam of the probe to control the relative phase between the reference and the signal. The diffracted signal and the reflected reference are collected at the detector.

The TTG signal will in principle have both real and imaginary field contributions due to "amplitude-grating" and "phase-grating" responses, respectively. The phase grating contributions contains decay components that correspond to thermal expansion and the imaginary part of the thermoreflectance and acoustic oscillations corresponding to the impulsive stimulation of surface acoustic waves (SAWs), whereas the amplitude-grating response only contains one term corresponding to the real part of the thermoreflectance [25]. Analysis of the amplitude-grating contribution is simpler due to the single contribution, and so this term was isolated during the measurements by optimizing the heterodyne phase to minimize the SAW signal which only appears in the phase-grating response [25].
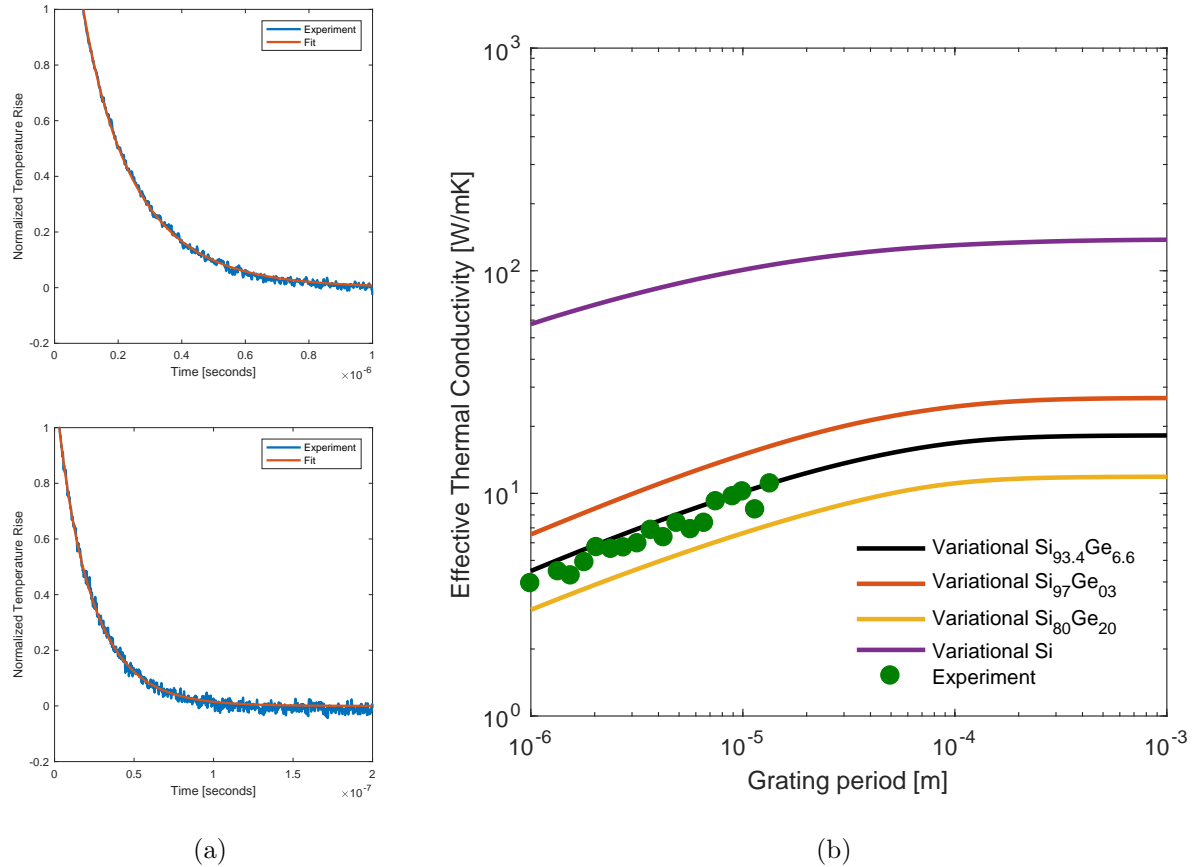
15

FIG. 6: (a) Raw experimental data for 6.6 μm (top) and 1.8 μm (bottom) grating periods with the fit obtained from Eq. 7. (b) Green circles correspond to measured TTG data for a range of grating periods, from 13.5 to 1 μm. The black line is the prediction from the variational solution with DFT properties as input, while the orange line (yellow line, purple line) corresponds to the variational prediction for $Si_{97}Ge_3$ ($Si_{80}Ge_{20}$, Si).

C. Results

All measurements of the $Si_{93.4}Ge_{6.6}$ sample were conducted at room temperature. Figure 6a shows two examples of raw TTG data along with the fits obtained from using Eq. 7. These fits yield an effective thermal conductivity as shown in Figure 6b alongside the prediction from the variational solution using properties obtained from first principle calculations following Section II. We have used an optical penetration depth of 1500 nm, according to [34]. The effect of uncertainty in the penetration depth is presented in the supplementary material. There is good agreement between theory and experiment, which persists for a

16

range of grating periods, from ~ 13.5 to 1 μm. Example fits of the TTG data with comparisons to the variational predictions are found in the supplementary material.

IV. DISCUSSION AND OUTLOOK

To review, we calculated the first principles phonon properties to match the exact composition of the sample studied experimentally. We then used these properties and the variational solution to the RTA-BTE to predict (without any fitting parameters) the recorded observable of TTG experiments, the temperature decay. In doing so, we report excellent agreement between the observables and effective thermal conductivities of theory and experiment. In this section, we draw on past interpretations to provide some context for this work.

As mentioned earlier, one of the first explanations of size effects in SiGe grew out of the observation of frequency dependence in TDTR measurements [8]. This explanation relied on the application of thermal penetration depth, $L_{tpd} \sim \sqrt{\frac{\alpha_{bulk}}{\omega}}$, as a heuristic approximation to estimate the magnitude of the deviation from a bulk thermal conductivity. For $Si_{93.4}Ge_{6.6}$, $\alpha_{bulk} = 1.2358\text{E-5}$ m^2/s, with 10 MHz, yields a $L_{tpd} \sim 1$ μm. Under this approximation, we can take the MFP thermal conductivity accumulation function at 1 μm, yielding $0.4k_{bulk} = 7.3$ W/mK [38]. If we apply the same reasoning to our TTG measurements we arrive at a clear inconsistency: $\lambda = 1$ μm yields $0.25k_{bulk} = 4.5$ W/mK, indicating that the MFP thermal conductivity accumulation function alone is insufficient to estimate the deviation from bulk. The next natural step in the interpretation of deviations from bulk required theory to go beyond the Heaviside cutoff of the thermal penetration depth and obtain a gray suppression function, $S_{gray}(\eta_\omega)$, from solving the gray BTE [39–41]

$$S_{gray}(\eta_\omega) = \frac{3}{\eta_\omega^2} \left(1 - \frac{\arctan(\eta_\omega)}{\eta_\omega} \right) \left(\frac{\eta_\omega}{\arctan(\eta_\omega)} \right). \tag{24}$$

This function is then used as a kernel in the effective thermal conductivity integral, i.e., $k_{eff,gray} = \frac{1}{3} \int_0^{\omega_m} C_\omega v_\omega \Lambda_\omega S_{gray}(\eta_\omega) d\omega$. This picture has also turned out to be an oversimplification, since the fully spectral solution to the BTE has no suppression function due to the presence of the denominator term in Eq. 20. The presence of this term is a general feature of effective thermal conductivity expressions that is not specific to the reflection mode TTG geometry [28, 31]. Our work confirms this fact by demonstrating that a fully spectral solu-
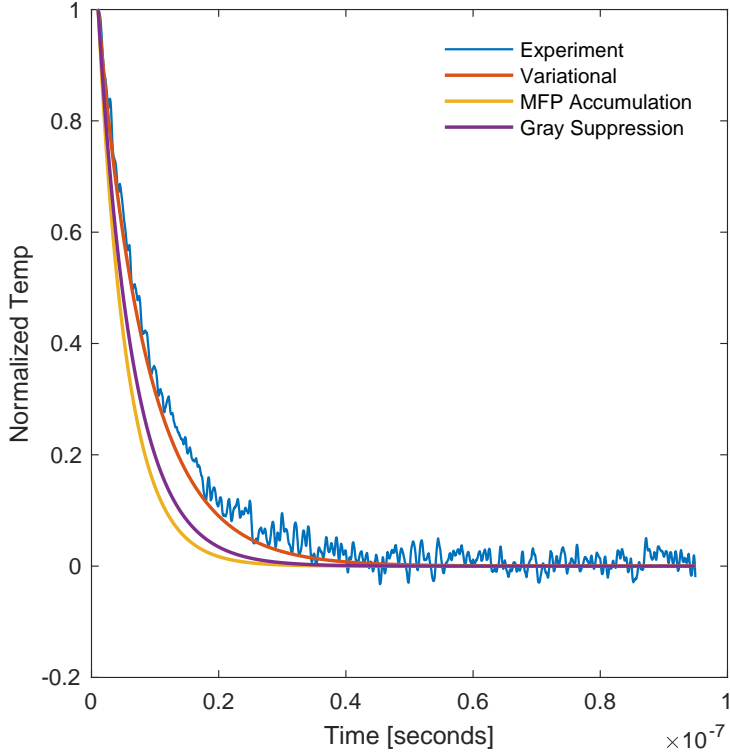
FIG. 7: Comparison between the predictions from the variational approach to using the MFP accumulation function or the gray suppression function for one-dimensional TTG (Eq. 24) [31] to estimate the effective thermal conductivity at 1.00 μm grating period.

tion to the BTE is required to characterize experimental observables. The progression from thermal penetration depth to gray suppression to fully spectral interpretations in the context of reflection TTG is shown in Figure 7. While the gray BTE solution has been used to provide suppression functions for the MFP reconstruction problem [1, 39], we demonstrate that this assumption is invalid. Extending the MFP reconstruction problem to allow for fully spectral solutions is the subject of future work.

In contrast to the interpretation of thermal penetration depth of TDTR, the length scales in TTG do not depend on the intrinsic value of a material's transport coefficient, and are therefore physically well-defined independent variables. Although the information concerning the optical penetration depth is required, this is well within current characterization technology [42]. Given that the variational solutions to the 1D and surface heating TTG geometries predict approximately the same effective thermal conductivity dependence on

grating period, we have obtained estimates for the regimes in which the experiment is expected to match theory (i.e., when q/β is not much less than 1). In doing so, we have presented a theoretical framework that is testable, given that experimental deviations from theory can be understood as departures from the approximations used in this work: the VCA, the RTA-BTE and the specific trial solution for the temperature profile used in the variational method. These approximations can be lifted and are left for future work. With the methodology presented here, the TTG can be used to study in-plane transport in opaque thin films that require a supporting substrate.

While TDTR measurements are sensitive to the cross-plane transport, the TTG provides a complementary tool for measuring in-plane transport. The variational method can be extended to more complicated geometries, such as layered systems with interfaces, ideally suited for providing insight into the interpretations of TDTR and TTG measurements. Such an extension would provide a path towards unifying the interpretations of the measurements from TDTR and TTG.

V.   CONCLUSION

Our TTG experimental results augmented with DFT-based modeling and the variational BTE solution indicate that this experimental geometry is capable of meeting the predictive criteria necessary for studying size effects on thermal transport in complex materials, such as the SiGe alloy studied here. Interesting questions can now be asked, such as in what systems or at what length scales can we expect to find a breakdown of the VCA? Moreover, this geometry will likely prove useful in the study of systems where the relaxation time approximation fails, such as graphene, graphite and diamond. The TTG experiment provides a path towards tabletop studies of the microscopic properties of thermal transport.

VI.   ACKNOWLEDGMENTS

_____

[1] Y. Hu, L. Zeng, A. J. Minnich, M. S. Dresselhaus, and G. Chen, Nature nanotechnology **10**, 701 (2015).

[2] J. Cuffe, J. K. Eliason, A. A. Maznev, K. C. Collins, J. A. Johnson, A. Shchepetov, M. Prunnila, J. Ahopelto, C. M. S. Torres, G. Chen, *et al.*, Physical Review B **91**, 245423 (2015).

[3] J. A. Johnson, J. K. Eliason, A. A. Maznev, T. Luo, and K. A. Nelson, Journal of Applied Physics **118**, 155104 (2015).

[4] H. Stohr and W. Klemm, Z. Anorg. Chem **241**, 305 (1939).

[5] A. M. Toxen, Physical Review **122**, 450 (1961).

[6] B. Abeles, D. Beers, G. D. Cody, and J. Dismukes, Physical review **125**, 44 (1962).

[7] B. Abeles, Physical Review **131**, 1906 (1963).

[8] Y. K. Koh and D. G. Cahill, Physical Review B **76**, 075207 (2007).

[9] C. A. da Cruz, W. Li, N. A. Katcho, and N. Mingo, Applied Physics Letters **101**, 083108 (2012).

[10] B. Vermeersch, J. Carrete, N. Mingo, and A. Shakouri, Physical Review B **91**, 085202 (2015).

[11] B. Vermeersch, A. M. Mohammed, G. Pernot, Y. R. Koh, and A. Shakouri, Physical Review B **91**, 085203 (2015).

[12] C. Hua, X. Chen, N. K. Ravichandran, and A. J. Minnich, arXiv preprint arXiv:1612.08401 (2016).

[13] R. Wilson and D. G. Cahill, Nature communications **5** (2014).

[14] D. Broido, A. Ward, and N. Mingo, Physical Review B **72**, 014308 (2005).

[15] D. Broido, M. Malorny, G. Birner, N. Mingo, and D. Stewart, Applied Physics Letters **91**, 231922 (2007).

[16] K. Esfarjani, G. Chen, and H. T. Stokes, Physical Review B **84**, 085204 (2011).

[17] L. Paulatto, F. Mauri, and M. Lazzeri, Physical Review B **87**, 214303 (2013).

[18] W. Li, J. Carrete, N. A. Katcho, and N. Mingo, Computer Physics Communications **185**, 1747 (2014).

[19] J. Garg, N. Bonini, B. Kozinsky, and N. Marzari, Physical review letters **106**, 045901 (2011).

[20] G. Antonius and S. G. Louie, Physical Review Letters **117**, 246401 (2016).

20

[21] S.-i. Tamura, Physical Review B **27**, 858 (1983).

[22] T. Feng, B. Qiu, and X. Ruan, Physical Review B **92**, 235206 (2015).

[23] D. Feldman, M. Ashkin, and J. H. Parker Jr, Physical Review Letters **17**, 1209 (1966).

[24] Z. Sui, H. H. Burke, and I. P. Herman, Physical Review B **48**, 2162 (1993).

[25] J. A. Johnson, A. A. Maznev, M. T. Bulsara, E. A. Fitzgerald, T. Harman, S. Calawa, C. Vineis, G. Turner, and K. A. Nelson, Journal of Applied Physics **111**, 023503 (2012).

[26] A. Majumdar, Journal of Heat Transfer **115**, 7 (1993).

[27] C. Hua and A. J. Minnich, Physical Review B **90**, 214306 (2014).

[28] K. C. Collins, A. A. Maznev, Z. Tian, K. Esfarjani, K. A. Nelson, and G. Chen, Journal of Applied Physics **114**, 104302 (2013).

[29] J.-P. M. Péraud and N. G. Hadjiconstantinou, Physical Review B **84**, 205331 (2011).

[30] J.-P. M. Péraud and N. G. Hadjiconstantinou, Applied Physics Letters **101**, 153114 (2012).

[31] V. Chiloyan, L. Zeng, S. Huberman, A. A. Maznev, K. A. Nelson, and G. Chen, Physical Review B **93**, 155201 (2016).

[32] V. Chiloyan, L. Zeng, S. Huberman, A. A. Maznev, K. A. Nelson, and G. Chen, Journal of Applied Physics **120**, 025103 (2016).

[33] F. Yang and C. Dames, Physical Review B **87**, 035437 (2013).

[34] R. Braunstein, A. R. Moore, and F. Herman, Physical Review **109**, 695 (1958).

[35] M. Currie, S. Samavedam, T. Langdo, C. Leitz, and E. Fitzgerald, Applied Physics Letters **72**, 1718 (1998).

[36] A. Maznev, K. Nelson, and J. Rogers, Optics letters **23**, 1319 (1998).

[37] A. Vega-Flick, J. Eliason, A. Maznev, A. Khanolkar, M. Abi Ghanem, N. Boechler, J. Alvarado-Gil, and K. Nelson, Review of Scientific Instruments **86**, 123101 (2015).

[38] By this same argument, frequency dependence should also be observed in silicon with $\alpha_{bulk} =$ 8.8E-5 m^2/s, which at 10 MHz, yields a $L_{tpd} \sim 3$ um and $\sim 0.7 k_{bulk} = 98$ W/mK from the MFP accumulation function [16], but $k_{exp} > 120$ W/mK for the same frequency range is often reported [13, 43]. The reason for this discrepancy remains an open question in the TDTR literature [12, 13, 44–46]. For example, the results of Hua et al. [12] and Wilson et al. [13] suggest that the reported thermal conductivity obtained from a TDTR measurement is dependent upon the interface conductance, indicating that this thermal conductivity can no longer be interpreted as an intrinsic property of the material.

[39] A. J. Minnich, Physical review letters **109**, 205901 (2012).

[40] K. Regner, A. J. McGaughey, and J. A. Malen, Physical Review B **90**, 064302 (2014).

[41] L. Zeng, K. C. Collins, Y. Hu, M. N. Luckyanova, A. A. Maznev, S. Huberman, V. Chiloyan, J. Zhou, X. Huang, K. A. Nelson, *et al.*, Scientific reports **5**, 17131 (2014).

[42] T. Fuyuki, H. Kondo, T. Yamazaki, Y. Takahashi, and Y. Uraoka, Applied Physics Letters **86**, 262108 (2005).

[43] R. Wilson and D. G. Cahill, Applied Physics Letters **107**, 203112 (2015).

[44] D. Ding, X. Chen, and A. Minnich, Applied Physics Letters **104**, 143104 (2014).

[45] B. Vermeersch and A. Shakouri, arXiv preprint arXiv:1602.05387 (2016).

[46] J. L. Braun and P. E. Hopkins, Journal of Applied Physics **121**, 175107 (2017).